Promising TMDC-like optical and excitonic properties of the $TiBr_2$ 2H monolayer†

André L. de O. Batista,[a] João Marcos T. Palheta,[b] Maurício J. Piotrowski,*[c] Celso R. C. Rêgo,[d] Diego Guedes-Sobrinho[e] and Alexandre C. Dias*[f]

The presented simulation protocol provides a solid foundation for exploring two-dimensional materials. Taking the $TiBr_2$ 2H monolayer as an example, this material displays promising TMDC-like optical and excitonic properties, making it an excellent candidate for optoelectronic and valleytronic applications. The direct band gap semiconductor (1.19 eV) is both structurally and thermodynamically stable, with spin–orbit coupling effects revealing a broken mirror symmetry in the K and K′ valleys of the band structure, as confirmed by opposite values of the Berry curvature. A direct and bright exciton ground state was found, with an exciton binding energy of 0.56 eV. The study also revealed an optical helicity selection rule, suggesting selectivity in the valley excitation by specific circular light polarizations.

1. Introduction

Since the experimental synthesis of graphene in 2004,[1] a vast field of materials science has opened up, exploring the properties of two-dimensional (2D) materials.[2,3] Transition-metal dichalcogenides (TMDCs) have been particularly interesting in the last decade,[4,5] especially concerning the 2H Mo and W-based monolayers,[6,7] which have shown intriguing valley physics. Recent research has also focused on new classes of 2D materials, such as transition-metal dihalides (TMDHs),[8–10] which are promising candidates for further exploration.

The TMDCs possess valley-physics and excitonic effects that make them useful for several applications in nanoelectronics. These include photovoltaic generation,[6,11] spintronic devices,[12] qubit generation,[13,14] and more. Combined with spin–orbit coupling effects, the 2H structure symmetry allows access to the valley degrees of freedom through selected optical helicity.[15] This enables the probing and manipulation of charge carriers in both valleys. Our investigation focuses on searching for new materials with promising TMDC-like optical and excitonic properties within 2H monolayer systems based on the TMDH family.[8,9] This could lead to the future design of spintronic and valleytronic devices.[16,17]

Theoretical investigations have shown that TMDHs, such as the PbI_2 single layer, have stable and attractive properties with exciton and spin–orbit coupling effects,[18,19] making them candidate materials with similar or superior properties to TMDCs. However, research on group IV elements (Ti, Zr, Hf) in the formula MX_2 (where M is a transition-metal and X is Cl, Br, I) has been limited to Janus TiXY 2H monolayers and their electronic properties, valley physics, and Berry curvature.[10] This study presents a proof of concept for the $TiBr_2$ 2H monolayer's structural, stability, electronic, optical, and excitonic properties. This system exhibits similar valley physics to that of Mo and W TMDC 2H monolayers, which may have similar behavior and lead to the same set of applications.

2. Theoretical methodology and computational details

To obtain the properties of the $TiBr_2$ 2H monolayer, we have proposed a calculation protocol as summarized in Fig. 1(a). The atomic configuration of the proposed candidate is given by a monolayer that has a honeycomb pattern, similar to graphene and MoS_2 2H monolayers, as can be seen in Fig. 1(b) and (c), where the Ti atoms are sandwiched between two Br layers, in the same way as the MoS_2 2H monolayer. Structural optimization and total energy calculations were performed through density functional theory (DFT)[20,21] as implemented in the Vienna *Ab initio* Simulation Package (VASP).[22,23] The electronic and structural properties were described within the

[a]*Institute of Physics, University of Brasília, 70919-970 Brasília, DF, Brazil*
[b]*Department of Physics, Federal University of Pelotas, PO Box 354, 96010-900 Pelotas, RS, Brazil*
[c]*Department of Physics, Federal University of Pelotas, PO Box 354, 96010-900 Pelotas, RS, Brazil. E-mail: mauriciomjp@gmail.com*
[d]*Institute of Nanotechnology Hermann-von-Helmholtz-Platz, Karlsruhe Institute of Technology, 76021 Karlsruhe, Germany*
[e]*Chemistry Department, Federal University of Paraná, 81531-980 Curitiba, PR, Brazil*
[f]*Institute of Physics and International Center of Physics, University of Brasília, 70919-970 Brasília, DF, Brazil. E-mail: alexandre.dias@unb.br*

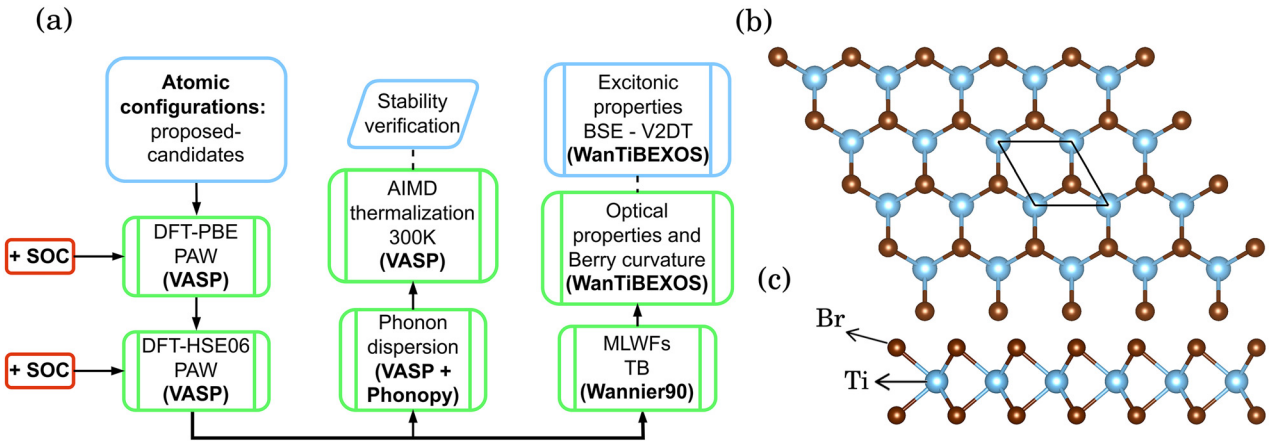

Fig. 1 (a) Calculation protocol flowchart applied to obtain the $TiBr_2$ 2H monolayer properties, together with the crystal structure: (b) top view and (c) side view.

scope of the semilocal exchange–correlation functional *via* the generalized gradient approximation[24] as proposed by Perdew–Burke–Ernzerhof (PBE).[25] However, as known from the literature,[26,27] the DFT–PBE framework can underestimate some electronic properties such as the bandgap due to self-interaction problems and a bad description of weak interactions;[28–30] therefore, we adopted the screened Coulomb hybrid exchange–correlation functional, as proposed by Heyd–Scuseria–Ernzerhof (HSE06).[31,32]

We incorporated spin–orbit coupling (SOC) effects into the plain DFT treatment using the scalar-relativistic approximation to understand the valley physics and its corresponding spin–valley configurations.[33] To achieve accurate results, SOC was considered for the valence states in both the DFT–PBE and DFT–HSE06 calculations using the second-variational approach.[34] The number of bands for these calculations was increased to twice the number of electrons.[6] The KS equations were solved using the all-electron projector augmented wave (PAW) method,[35,36] where the KS states were expanded into plane-waves. We obtained the equilibrium structure by performing stress-tensor optimization and atomic force minimization using a cutoff energy of 767.55 eV for the equilibrium configuration and 431.75 eV for the other properties. We achieved convergence once the atomic forces on each atom were smaller than 0.01 eV $Å^{-1}$ with a total energy convergence of 10^{-6} eV.

In the study, a *k*-mesh of 16 × 16 × 1 was used for the Brillouin zone (BZ) integration for all electronic properties, except for density of states (DoS), which required a higher 32 × 32 × 1 *k*-mesh. To avoid unwanted interactions between the $TiBr_2$ 2H monolayer and its periodic images in the $\hat{z}$ direction, a vacuum thickness of 16 Å was employed since the monolayer was built with *xy* periodicity. The phonon dispersion was obtained using VASP (DFT–PBE) and Phonopy packages,[37] using the finite displacement method, with a 4 × 4 × 1 supercell and a 4 × 4 × 1 *k*-mesh. Furthermore, the stability verification process was supplemented by *ab initio* molecular dynamics (AIMD) simulations using the Nosé thermostat for approximately 5 ps, with a time step of 1 fs at 300 K thermalization.

We employed the WanTiBEXOS (**https://wantibexos.readthedocs.io/**) package developed in our group[38] to solve the Bethe–Salpeter equation (BSE)[39] using a tight-binding Hamiltonian. This code allows us to compute the excitonic and optical properties and the computation of the Berry curvature quickly. We used a maximally localized Wannier function TB Hamiltonian (HSE06 + SOC) obtained using the Wannier90 package,[40] considering the d projections for Ti and p projections for Br. The BSE was solved using a 2D Coulomb truncated potential (V2DT)[41] with 2 conduction and 2 valence bands. A *k*-mesh of 40 × 40 × 1 was employed from dielectric functions with a smearing of 0.02 eV. The optical activity and dichroism in the first BZ, at the independent-particle approximation (IPA) level, was obtained according to the work of Lu *et al.*,[42] adopting a single caveat in the circular dichroism, where the linear polarization was changed by circular polarization in the mathematical expression. A *k*-mesh of 133 × 133 × 1 was adopted by considering the same number of conduction and valence states as that used for BSE calculation so that this protocol was repeated for the *k*-mesh used for Berry curvature.

3. Results and discussion

3.1. Crystal structure and structural stability

The obtained crystalline structure for the $TiBr_2$ 2H monolayer has a lattice parameter of 3.47 Å, with a Ti–Br distance of 2.47 Å, and a top–bottom Br distance of 3.17 Å. We adopted a two-step stability verification process to ensure the structure is thermodynamically stable. Firstly, the phonon dispersion was calculated, and no imaginary frequency was observed, indicating the stability of the monolayer (Fig. 2(a)). Vibrational frequencies not higher than 10 THz were also obtained, as shown in Fig. 2(b). Second, the AIMD thermalization process at 300 K

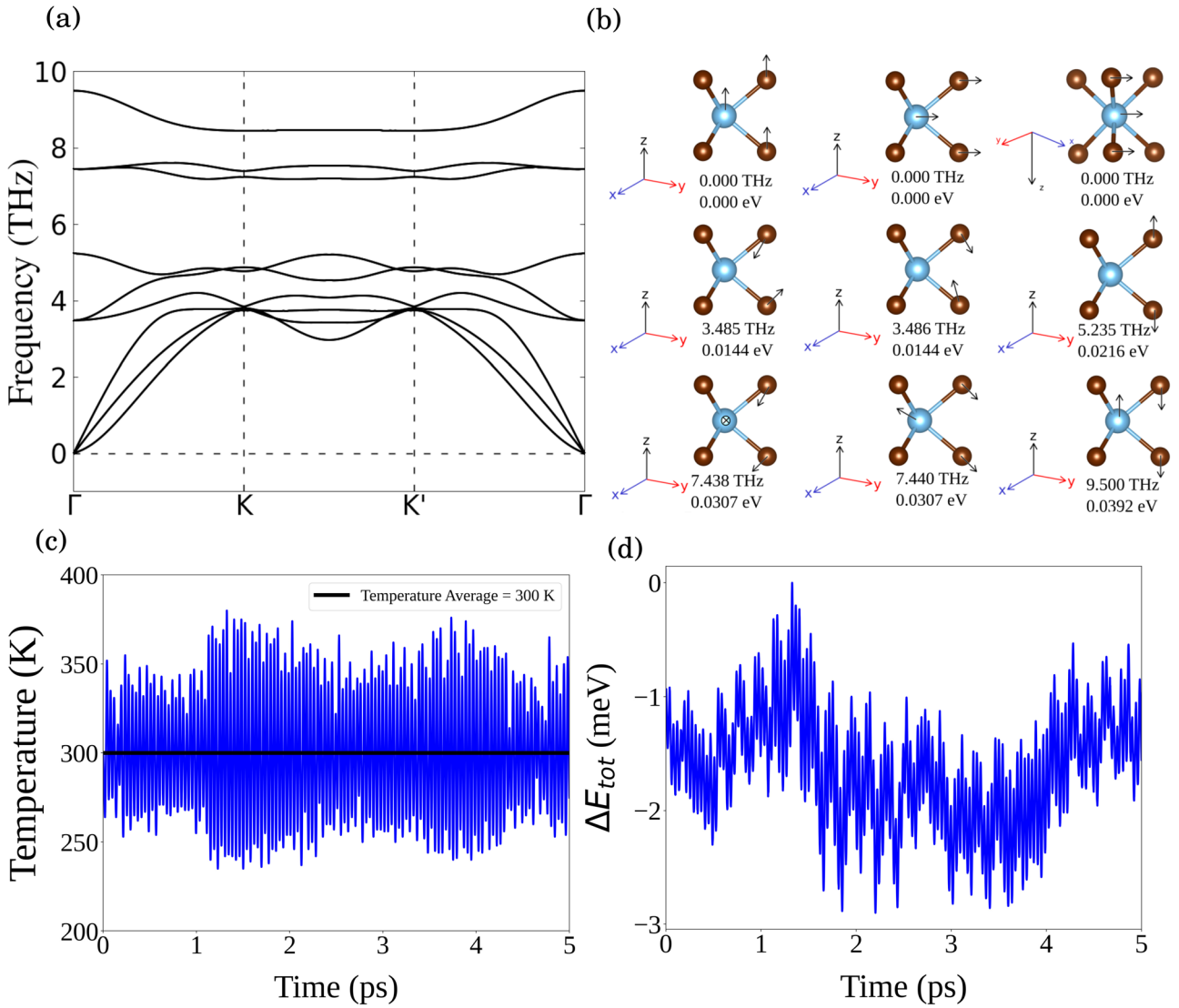

Fig. 2 (a) Phonon dispersion, (b) phonon vibrational modes in Γ, (c) AIMD simulation (thermalization): temperature *versus* time (ps) and (d) relative total energy (ΔE_{tot}) *versus* time (ps) for $TiBr_2$ 2H monolayer.

was observed. The structural motif of the $TiBr_2$ 2H monolayer was found to be preserved against temperature variations at the potential energy surface, as shown in Fig. 2(c) and (d).

To complement the energy stability analyses, we have calculated the cohesion energy and some derived thermodynamic properties that help confirm the stability of the $TiBr_2$ 2H monolayer. These analyses can be found in the ESI.†

3.2. Electronic properties

In Fig. 3(a), we can see that the semiconductor character of the DoS is mainly due to the Ti d-orbitals and Br p-orbitals around the Fermi level. These contributions were projected to obtain the MLWF–TB Hamiltonian using the Wannier90 code. Moving on to Fig. 3(b), we compare the electronic band structure obtained by DFT–PBE and DFT–PBE + SOC to understand the magnitude of the SOC effect. At the DFT–PBE level, we observe an indirect fundamental band gap of 0.80 eV, with the VBM in the K or K′ valleys and the CBM between the valleys and Γ point. The direct band gap in the K or K′ valley has a value of 0.98 eV. When the SOC is taken into account, the fundamental band gap changes to 0.76 eV and the direct band gap to 0.94 eV. Although the electronic band gap changes are weak, the main SOC effects are related to changes in other electronic band-structure characteristics. The spin degeneracy breaking around the K and K′ valleys in the valence bands is one of the significant effects, making these valleys energetically equivalent but with opposite spin configurations. This same behavior has been extensively explored in the context of Mo-based TMDCs.[43–46]

In Fig. 3(c), we can see that the DFT–PBE calculation underestimates the electronic band gap compared to the DFT–HSE06 + SOC calculation. The red dashed lines in the figure show the band structure obtained *via* DFT–HSE06 + SOC, while the solid black lines show the band structures obtained

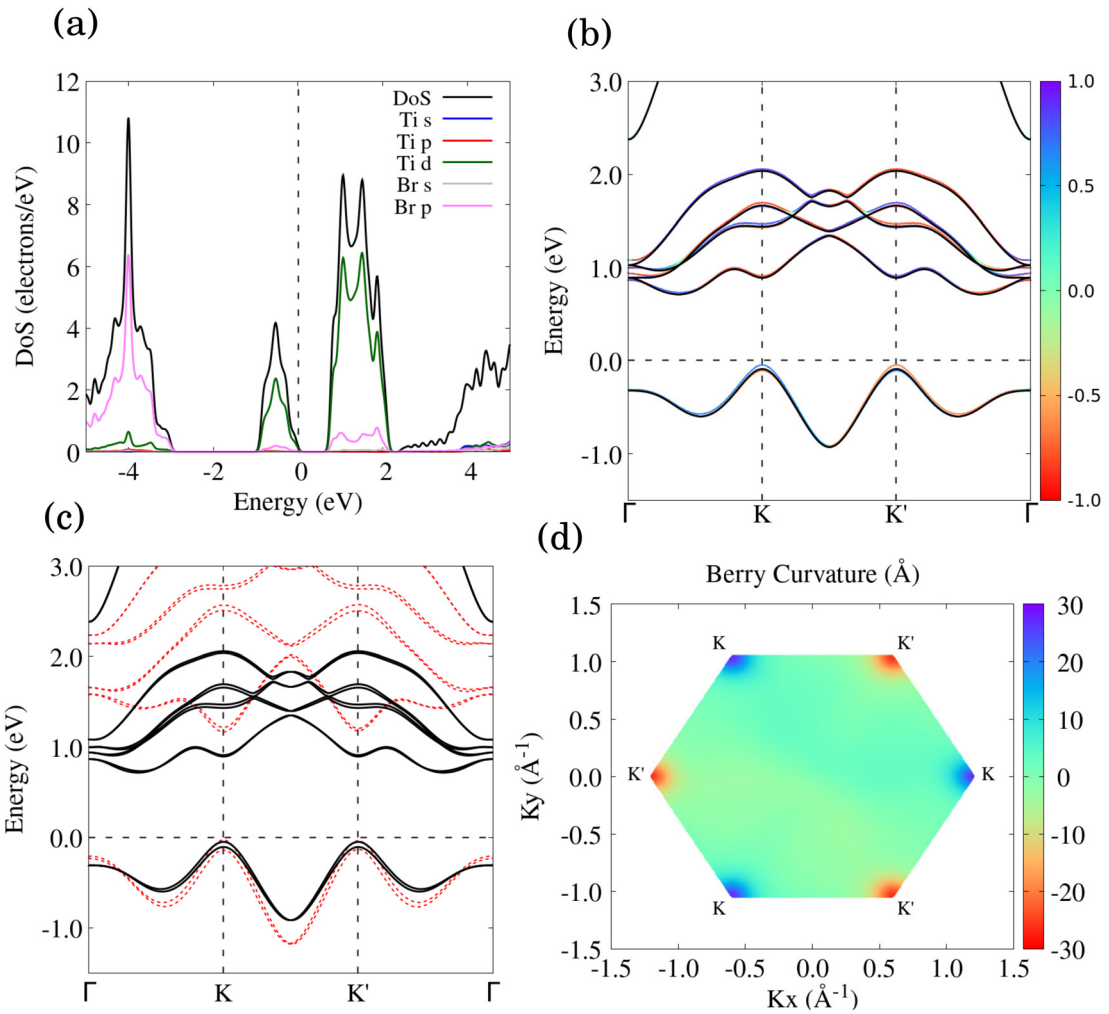

Fig. 3 (a) Density of states (DoS) from DFT–PBE; (b) band structure from DFT–PBE (black curves) and DFT–PBE + SOC (color curves). The color code represents the average value of S_z spin operator; (c) comparison between DFT–PBE + SOC bands (black solid curves) and DFT–HSE06 + SOC bands (red dashed curves) of $TiBr_2$ 2H monolayer. (d) Total Berry curvature (DFT–HSE06 + SOC MLWF–TB parametrization) was obtained in the first BZ. The Fermi level is set at 0 eV.

from DFT–PBE + SOC. Using the HSE06 hybrid functional calculation, the fundamental band gap is corrected to 1.19 eV and becomes direct at the K and K′ valleys. The spin-degeneracy break in both valleys is slightly increased due to the hybrid functional correction. This improvement behavior has been observed in TMDC monolayers based on Mo and W.[6] To complement this finding, Fig. 3(d) shows the total Berry curvature in the first BZ, which verifies the non-equivalence of the K and K′ valleys with opposite signs on Berry's curvature. This result is widely reported in TMDC monolayers based on Mo and W.[47,48] It resembles the outcome reported by Wang *et al.*,[10] which can be directly associated with a valley selection rule by optical helicity, a fundamental mechanism in the valleytronic field.

3.3. Optical and excitonic properties

Fig. 4 shows the optical activity in the BZ, which was calculated in the IPA regime by summing the oscillator strength for all possible optical transitions. The optical activity was considered for the first two conduction and valence bands for each *k*-point. Panels (a) and (b) show the optical activity for circular light polarization, which explains the optical valley selection rule. Valley K is excited only by σ^+ light polarization, whereas valley K′ is excited only by σ^- polarization. Panel (c) presents the optical circular dichroism, which indicates how the optical excitation throughout the entire BZ is divided by the optical helicity. The optical activation of both valleys is verified through linear light polarization, as shown in panels (d) and (e). However, the optical activity in the BZ has a different pattern for each linear light polarization, resulting in the linear optical dichroism illustrated in panel (f). Finally, we can observe that the optical activity in the K and K′ valleys by circular polarization is almost twice the intensity by linear polarization.

As shown in Fig. 5(a), the excitonic band structure displays a direct (in Γ) ground state with an energy of 0.65 eV. The for-

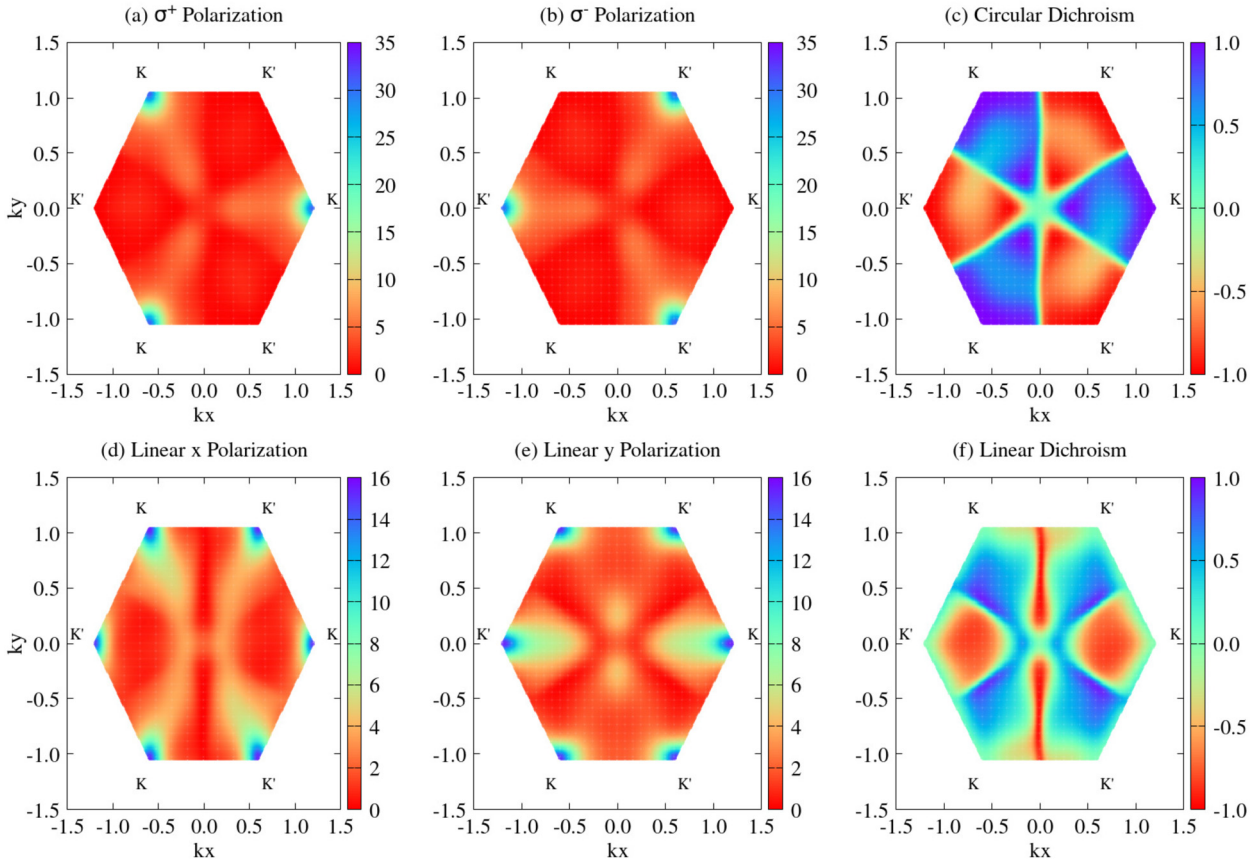

Fig. 4 Optical activity obtained in the first BZ, with circular light polarization (a) and (b), with linear light polarization (d) and (e), circular (c) and linear (f) optical dichroism in the first BZ. All calculations were performed with DFT–HSE06 + SOC and MLWF–TB parametrization.

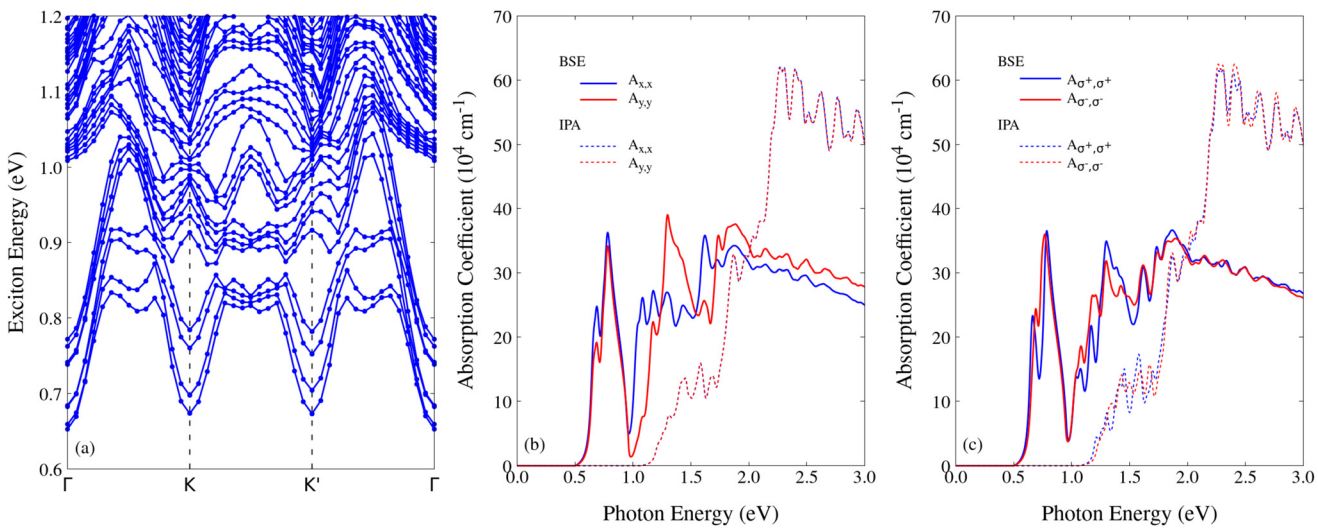

Fig. 5 (a) Exciton band structure (DFT–HSE06 + SOC–BSE) and (b) optical absorption coefficient at IPA (dashed curves) and BSE (solid curves) levels, considering the linear light polarization at $\hat{x}$ (blue curves) and $\hat{y}$ (red curves) directions, (c) same as (b) but with circular light polarization σ^+ (blue curves) and σ^- (red curves).

mation of this ground state is due to the creation of electron–hole pairs with the same momentum k. Its exciton binding energy is 0.56 eV, obtained by subtracting the fundamental band gap from the exciton ground state. This binding energy is justified by the monolayer quantum confinement in the $\hat{z}$ direction. The exciton band structure dispersion for the $TiBr_2$ 2H monolayer is similar to that reported in the work by Wu *et al.*[4] for the MoS_2 monolayer case. In both systems, the

exciton ground state is observed at Γ, and two other local minima are observed at the K and K′ valleys.

Additionally, an indirect higher-energy exciton is observed in both systems. Fig. 5(b) and (c) show the absorption spectra for linear and circular light polarizations, respectively. The solid lines represent the spectra obtained using the Bethe–Salpeter equation. In contrast, the dashed lines represent the spectra obtained using the independent particle approximation. The spectra confirm that the exciton ground state is optically active (*i.e.*, bright). The effect of spin–orbit coupling can be observed in identifying excitons A and B with energies of 0.65 eV and 0.74 eV, respectively. These excitons are analogous to those observed in TMDC monolayers based on Mo and W. When quasi-particle effects are considered, the absorption intensities differ slightly depending on the incident light polarization. Still, the spectra are practically identical for circular or linear approximations in the IPA approximation.

4. Conclusions

This work has confirmed a simulation protocol that enables the exploration of promising 2D materials for optoelectronic applications, such as the $TiBr_2$ 2H monolayer, which has shown promising TMDC-like optical and excitonic properties. The protocol was based on first-principles approximations with a stability verification followed by a complete electronic/optical characterization. The $TiBr_2$ 2H monolayer is a semiconductor with a direct gap of 1.19 eV in the band structure's K and K′ valleys, both valleys with opposite spin configurations. Berry curvature has opposite values, showing a broken mirror symmetry similar to 2H TMDC monolayers. A higher exciton binding energy was found, with the exciton ground state being direct and bright. The SOC splitting effect leads to the bright A and B excitons. Optical activity analysis revealed a valley selection rule due to optical helicity, where each valley is excited by a specific circular light polarization, leading to a high circular optical dichroism in the BZ.

Moreover, this work has set the stage for an upcoming significant advancement by integrating the simulation protocol, as depicted in Fig. 1(a), into the Simstack[49,50] framework (**https://simstack.readthedocs.io/**). Workflows are becoming vital in computational simulations[51–53] since they easily merge methods from diverse fields into efficient workflows to tackle complex material characteristics. By incorporating the protocol into the Simstack framework, we aim to streamline the exploration and characterization of materials like the $TiBr_2$ 2H monolayer, discovering novel properties and potential applications in spintronic and valleytronic devices.

Author contributions

M. J. P. and A. C. D. conceptualized this research and guided the data analysis/interpretation. A. L. O. B. and J. M. T. P. performed the calculations and the preliminary formal analysis. C. R. C. R. and D. G.-S. contributed with extra calculations/analyses. All authors reviewed earlier drafts to produce the final version of the paper. M. J. P. and A. C. D. were responsible for funding acquisition and project administration.

Conflicts of interest

There are no conflicts to declare.

Acknowledgements

The authors are thankful for financial support from the National Council for Scientific and Technological Development (CNPq, grant numbers 307345/2021-1 and 408144/2022-0), Federal District Research Support Foundation (FAPDF, grant 00193-00001817/2023-43), the Coordination for Improvement of Higher Level Education (CAPES), the Rio Grande do Sul Research Foundation (FAPERGS), and the German Federal Ministry of Education and Research (BMBF) for financial support of the project Innovation-Platform MaterialDigital (**https://www.materialdigital.de**) through project funding FKZ number: 13XP5094A. Part of this work was performed on the HoreKa supercomputer funded by the Ministry of Science, Research and the Arts Baden-Württemberg and by the Federal Ministry of Education and Research. In addition, the authors thanks the "Centro Nacional de Processamento de Alto Desempenho em São Paulo" (CENAPAD-SP, UNICAMP/FINEP – MCTI project) for resources into the 897 and 570 projects, Lobo Carneiro HPC (NACAD) at the Federal University of Rio de Janeiro (UFRJ) for resources into 133 project CIMATEC SENAI at Salvador – BA, Brazil, for the partnership and support through the Atos Computer, and "Laboratório Central de Processamento de Alto Desempenho" (LCPAD) financed by FINEP through CT-INFRA/UFPR projects.

References

1 K. S. Novoselov, A. K. Geim, S. V. Morozov, D. Jiang, Y. Zhang, S. V. Dubonos, I. V. Grigorieva and A. A. Firsov, *Science*, 2004, **306**, 666–669.
2 Q. H. Wang, K. Kalantar-Zadeh, A. Kis, J. N. Coleman and M. S. Strano, *Nat. Nanotechnol.*, 2012, **7**, 699–712.
3 J. Kang, S. Tongay, J. Zhou, J. Li and J. Wu, *Appl. Phys. Lett.*, 2013, **102**, 4774090.
4 F. Wu, F. Qu and A. H. MacDonald, *Phys. Rev. B: Condens. Matter Mater. Phys.*, 2015, **91**, 075310.
5 J. H. Correa, A. C. Dias, L. Villegas-Lelovsky, J. Fu, L. Chico and F. Qu, *Phys. Rev. B*, 2020, **101**, 195422.
6 A. C. Dias, H. Bragança, J. P. A. de Mendonça and J. L. F. D. Silva, *ACS Appl. Energy Mater.*, 2021, **4**, 3265–3278.

7 N. Thomas, S. Mathew, K. M. Nair, K. O'Dowd, P. Forouzandeh, A. Goswami, G. McGranaghan and S. C. Pillai, *Mater. Today Sustainability*, 2021, **13**, 100073.
8 M. McGuire, *Crystals*, 2017, **7**, 121.
9 V. V. Kulish and W. Huang, *J. Mater. Chem. C*, 2017, **5**, 8734–8741.
10 Y. Wang, W. Wei, H. Wang, N. Mao, F. Li, B. Huang and Y. Dai, *J. Phys. Chem. Lett.*, 2019, **10**, 7426–7432.
11 C. M. O. Bastos, R. Besse, J. L. F. Da Silva and G. M. Sipahi, *Phys. Rev. Mater.*, 2019, **3**, 044002.
12 N. Zibouche, A. Kuc, J. Musfeldt and T. Heine, *Ann. Phys.*, 2014, **526**, 395–401.
13 J.-Y. Tsai, J. Pan, H. Lin, A. Bansil and Q. Yan, *Nat. Commun.*, 2022, **13**, 41467.
14 H. S. Borges, C. A. N. Júnior, D. S. Brandão, F. Liu, V. V. R. Pereira, S. J. Xie, F. Qu and A. M. Alcalde, *Phys. Rev. B*, 2023, **107**, 035404.
15 T. Cao, G. Wang, W. Han, H. Ye, C. Zhu, J. Shi, Q. Niu, P. Tan, E. Wang, B. Liu and J. Feng, *Nat. Commun.*, 2012, **3**, 1882.
16 T. Kurumaji, S. Seki, S. Ishiwata, H. Murakawa, Y. Tokunaga, Y. Kaneko and Y. Tokura, *Phys. Rev. Lett.*, 2011, **106**, 167206.
17 Y. Tokunaga, D. Okuyama, T. Kurumaji, T. Arima, H. Nakao, Y. Murakami, Y. Taguchi and Y. Tokura, *Phys. Rev. B: Condens. Matter Mater. Phys.*, 2011, **84**, 060406.
18 M. Zhou, W. Duan, Y. Chen and A. Du, *Nanoscale*, 2015, **7**, 15168–15174.
19 A. S. Toulouse, B. P. Isaacoff, G. Shi, M. Matuchová, E. Kioupakis and R. Merlin, *Phys. Rev. B: Condens. Matter Mater. Phys.*, 2015, **91**, 165308.
20 P. Hohenberg and W. Kohn, *Phys. Rev.*, 1964, **136**, B864–B871.
21 W. Kohn and L. J. Sham, *Phys. Rev.*, 1965, **140**, A1133–A1138.
22 G. Kresse and J. Hafner, *Phys. Rev. B: Condens. Matter Mater. Phys.*, 1993, **48**, 13115–13118.
23 G. Kresse and J. Furthmüller, *Phys. Rev. B: Condens. Matter Mater. Phys.*, 1996, **54**, 11169–11186.
24 J. P. Perdew, J. A. Chevary, S. H. Vosko, K. A. Jackson, M. R. Pederson, D. J. Singh and C. Fiolhais, *Phys. Rev. B: Condens. Matter Mater. Phys.*, 1992, **46**, 6671–6687.
25 J. P. Perdew, K. Burke and M. Ernzerhof, *Phys. Rev. Lett.*, 1996, **77**, 3865–3868.
26 A. J. Cohen, P. Mori-Sánchez and W. Yang, *Phys. Rev. B: Condens. Matter Mater. Phys.*, 2008, **77**, 115123.
27 J. M. Crowley, J. Tahir-Kheli and W. A. Goddard, *J. Phys. Chem. Lett.*, 2016, **7**, 1198–1203.
28 C. R. C. Rêgo, L. N. Oliveira, P. Tereshchuk and J. L. F. Da Silva, *J. Phys.: Condens. Matter*, 2016, **28**, 129501.
29 C. R. C. Rêgo, P. Tereshchuk, L. N. Oliveira and J. L. F. Da Silva, *Phys. Rev. B*, 2017, **95**, 235422.
30 C. R. C. Rêgo, L. N. Oliveira, P. Tereshchuk and J. L. F. Da Silva, *J. Phys.: Condens. Matter*, 2015, **27**, 415502.
31 J. Heyd, G. E. Scuseria and M. Ernzerhof, *J. Chem. Phys.*, 2003, **118**, 8207–8215.
32 A. V. Krukau, O. A. Vydrov, A. F. Izmaylov and G. E. Scuseria, *J. Chem. Phys.*, 2006, **125**, 224106.
33 T. Takeda, *Z. Phys. B: Condens. Matter Quanta*, 1978, **32**, 43–48.
34 D. D. Koelling and B. N. Harmon, *J. Phys. C: Solid State Phys.*, 1977, **10**, 3107–3114.
35 P. E. Blöchl, *Phys. Rev. B: Condens. Matter Mater. Phys.*, 1994, **50**, 17953–17979.
36 G. Kresse and D. Joubert, *Phys. Rev. B: Condens. Matter Mater. Phys.*, 1999, **59**, 1758–1775.
37 A. Togo and I. Tanaka, *Scr. Mater.*, 2015, **108**, 1–5.
38 A. C. Dias, J. F. Silveira and F. Qu, *Comput. Phys. Commun.*, 2023, **285**, 108636.
39 E. E. Salpeter and H. A. Bethe, *Phys. Rev.*, 1951, **84**, 1232–1242.
40 A. A. Mostofi, J. R. Yates, Y.-S. Lee, I. Souza, D. Vanderbilt and N. Marzari, *Comput. Phys. Commun.*, 2008, **178**, 685–699.
41 C. A. Rozzi, D. Varsano, A. Marini, E. K. U. Gross and A. Rubio, *Phys. Rev. B: Condens. Matter Mater. Phys.*, 2006, **73**, 205119.
42 J. Lu, F. Qu, H. Zeng, A. C. Dias, D. S. Bradão and J. Ren, *J. Phys. Chem. Lett.*, 2022, **13**, 5204–5212.
43 Y. Li, J. Ludwig, T. Low, A. Chernikov, X. Cui, G. Arefe, Y. D. Kim, A. M. van der Zande, A. Rigosi, H. M. Hill, S. H. Kim, J. Hone, Z. Li, D. Smirnov and T. F. Heinz, *Phys. Rev. Lett.*, 2014, **113**, 266804.
44 D. MacNeill, C. Heikes, K. F. Mak, Z. Anderson, A. Kormányos, V. Zólyomi, J. Park and D. C. Ralph, *Phys. Rev. Lett.*, 2015, **114**, 037401.
45 Y. Liu, Y. Gao, S. Zhang, J. He, J. Yu and Z. Liu, *Nano Res.*, 2019, **12**, 2695–2711.
46 A. C. Dias, H. Bragança, H. Zeng, A. L. A. Fonseca, D.-S. Liu and F. Qu, *Phys. Rev. B*, 2020, **101**, 085406.
47 W. Feng, Y. Yao, W. Zhu, J. Zhou, W. Yao and D. Xiao, *Phys. Rev. B: Condens. Matter Mater. Phys.*, 2012, **86**, 165108.
48 L. Xu, M. Yang, L. Shen, J. Zhou, T. Zhu and Y. P. Feng, *Phys. Rev. B*, 2018, **97**, 041405.
49 C. R. C. Rêgo, J. Schaarschmidt, T. Schlöder, M. Penaloza-Amion, S. Bag, T. Neumann, T. Strunk and W. Wenzel, *Front. Mater.*, 2022, **9**, 877597.
50 J. Schaarschmidt, J. Yuan, T. Strunk, I. Kondov, S. P. Huber, G. Pizzi, L. Kahle, F. T. Bolle, I. E. Castelli, T. Vegge, F. Hanke, T. Hickel, J. Neugebauer, C. R. C. Rêgo and W. Wentzel, *Adv. Energy Mater.*, 2021, 2102638.
51 L. O. de Araujo, C. R. C. Rêgo, W. Wenzel, D. N. Silveira, M. J. Piotrowski, F. P. Sabino, Y. Pramudya and D. Guedes-Sobrinho, *J. Comput. Chem.*, 2023, **44**, 1395–1403.
52 M. Mostaghimi, C. R. C. Rêgo, R. Haldar, C. Wöll, W. Wenzel and M. Kozlowska, *Front. Mater.*, 2022, **9**, 840644.
53 H. Pecinatto, C. R. C. Rêgo, W. Wenzel, C. A. Frota, B. M. S. Perrone, M. J. Piotrowski, D. Guedes-Sobrinho, A. C. Dias, C. Mota, M. S. S. Gusmão and H. O. Frota, *Sci. Rep.*, 2023, **13**, 17157.